Environmental Science Processes & Impacts

ROYAL SOCIETY OF CHEMISTRY

PAPER

View Article Online
View Journal

Cite this: DOI: 10.1039/d5em00868a

Effect of carbon black nanoparticles on the albumin secondary structure

Yuta Takahashi,[a] Samal Kaumbekova,[b] Naoya Sakaguchi,[a] Atsuto Onoda,[c] Toshiyuki Watanabe[ab] and Masakazu Umezawa *[abd]

Nano-particulate air pollutants—particularly fine particle matter (PM2.5)—may cause several health issues, such as the accumulation of misfolded proteins in developing brains. However, the physicochemical molecular mechanism underlying nanoparticle (NP) toxicity remains poorly understood. This study investigates the effects of carbon black (CB) NPs (CB-NPs), with different surface properties and particle sizes, on the secondary structure of bovine serum albumin (BSA) using Fourier transform infrared and circular dichroism (CD) spectroscopic techniques, complemented by molecular dynamics (MD) simulations. The BSA sample incubated with CB-NPs exhibited no significant change when analyzed with excess BSA unbound to the NPs; however, CD spectroscopy revealed that Printex 90—a CB-NP with a smaller primary particle size and a more defective graphene structure—induced a notable change in the secondary structure of the adsorbed BSA. This change was characterized by a decrease in α-helix content and an increase in β-sheets. MD simulations further supported these findings, signifying that BSA monomers were adsorbed onto the CB-NP surface, leading to restricted protein mobility. This study provides crucial molecular-level insight into the role of carbonaceous NPs in triggering protein unfolding, a crucial step in NP toxicity.

Received 24th October 2025
Accepted 19th April 2026

DOI: 10.1039/d5em00868a

rsc.li/espi

Environmental significance

Carbon black nanoparticles (CB-NPs) are a major component of fine particulate matter (PM2.5) that can cause health effects. Although the toxicological effects of such NPs have been reported, the specific molecular mechanism by which the environmental particles induce toxicity remains poorly understood. In this study, we investigated the changes in the secondary structure of albumin protein after incubation with CB-NPs, highlighting that those particularly with smaller primary particle size and more defective graphene structures can directly induce conformational changes in serum albumin, the most abundant protein in blood plasma. Our findings establish a direct link between the physicochemical properties of a common air pollutant and its potential to trigger protein denaturation. This research emphasizes the need for further investigations to understand the long-term effect of airborne NPs on *in vivo* protein conformation.

Introduction

Inhaled nanoparticles (NPs, <100 nm in diameter) come in contact with antioxidant lipids and pulmonary surfactants and can penetrate through the blood–air barrier of the lungs, subsequently interacting with plasma proteins.[1,2] Nanosized particulate matter can induce conformational changes in proteins, leading to loss of protein function, altered molecular interactions, and the initiation of inflammatory, allergic, or autoimmune reactions.[3,4] Carbon black NPs (CB-NPs)—a particulate air pollutant that adversely affects human health—are primary aerosols formed by the combustion of fossil fuels, biofuels, and biomass and are a major component of PM2.5.[5,6] Potential effects of particulate air pollutants to induce disease-like phenotypes on the brain have been noted.[7,8] Exposure to CB-NPs during the fetal period has adverse effects on the developing brain; these effects include the accumulation of misfolded proteins around blood vessels in the brain.[9,10] Such abnormal perivascular pathology is associated with enhanced endoplasmic reticulum stress in the perivascular cells,[11] denaturation of the perivascular macrophage, and persistent astrocyte activation.[12–14]

After reaching the bloodstream *via* various exposure routes,[15] NPs are transported by blood flow forces[16] and interact with blood proteins.[17] Proteins and other biomolecules compete to bind to the surface of NPs, forming NP–protein complexes. This NP–protein complex formation significantly influences the

[a]Department of Materials Science and Technology, Graduate School of Advanced Engineering, Tokyo University of Science, 6-3-1 Niijuku, Katsushika, Tokyo 125-8585, Japan. E-mail: masa-ume@rs.tus.ac.jp
[b]Department of Medical and Robotic Engineering Design, Faculty of Advanced Engineering, Tokyo University of Science, 6-3-1 Niijuku, Katsushika, Tokyo 125-8585, Japan
[c]Department of Toxicology and Health Science, Faculty of Pharmaceutical Sciences, Sanyo-Onoda City University, 1-1-1 Daigaku-dori, Sanyo-Onoda City, Yamaguchi 756-0884, Japan
[d]Division of Smart Healthcare Engineering, Research Institute for Science and Technology, Tokyo University of Science, 2641 Yamazaki, Noda, Chiba, Japan

biodistribution, intracellular behavior, and biological activity of NPs, making it a crucial factor in evaluating NP toxicity.[18] Depending on temperature, pH, and physicochemical properties of proteins and NP surfaces, proteins might be adsorbed onto NPs *via* complex mechanisms.[19–21] A broad understanding of NP–protein interactions is crucial for various applications, such as in the food industry, drug delivery, and medical biology.

Interactions between proteins, including fibrinogen, transferrin, and lipase, with various NPs (gold, iron oxide, and organic ones like polystyrene) have been previously reported.[22–24] When NPs are dispersed in serum, albumin diffuses rapidly and adsorbs onto their surfaces, followed by replacement by higher molecular weight proteins, such as fibrinogen and globulin.[20,25–28] Moreover, when albumin is adsorbed on hydrophobic surfaces of NPs even *via* weak binding with end-on orientations, intraprotein hydrophobic and electrostatic interactions prevent its replacement by larger proteins.[29] Electrostatic interactions between bovine serum albumin (BSA) and amine- or carboxy-modified NP surfaces can regulate the NP–protein interactions, increasing the α-helix content in BSA.[30] While citrate-coated gold and silver NPs disrupt the α-helix structure of BSA, the effect can be partially suppressed by a polymer coating on silver NPs.[31] For oxide NPs, such as SiO_2 and TiO_2, the amide I and II bands of BSA and human serum albumin shift to higher wavenumbers, indicating alterations in their secondary structure.[32] The effects of CeO_2 on the amide I band in the Fourier transform infrared (FTIR) spectra of BSA vary depending on the surface modification.[33] Studies have also reported the adsorption of BSA on Al_2O_3 NPs, mediated by secondary structure changes detectable in the FTIR spectra.[34]

It has been pointed out that the toxicity of combustion-derived fine particles and soot depends not only on the size of the particles but also on their surface chemistry;[62] therefore, it is essential to carefully consider the interactions between these physicochemical properties and target molecules. The amount of protein adsorption and the rearrangement of secondary structures are strongly controlled by NP surface coatings and ligand orientation.[63,64] Studies using inorganic NPs such as iron oxide,[65,66] gold,[67,68] and various metal oxides (ZnO, TiO_2, and CeO_2)[33,69] have also demonstrated the adsorption of albumin and the associated structural denaturation. The formation of such protein coronas not only alters the dispersion and aggregation of NPs but also serves as a factor influencing cellular uptake mechanisms.[70,71] This phenomenon has been reported for various NPs; for example, even in the case of lipid NPs administered into the bloodstream, the corona formed by the dynamic adsorption of apolipoproteins onto the surface controls delivery to target cells *via* specific receptors and *in vivo* distribution.[72]

As such, recent studies suggested that carbonaceous NPs bind to BSA primarily through hydrophobic forces. BSA coated on the CB-NP surface nearly retains its native conformation, with only a slight reduction in the α-helix content.[35] Fluorescence spectroscopy has revealed that the ultraviolet (UV) fluorescence of BSA quenches with increasing concentrations of single-walled carbon nanotubes.[36] Moreover, a decrease in the α-helix content of BSA and partial unfolding in the presence of graphene oxide was revealed through circular dichroism (CD) analysis.[37] Although CB-NPs have been widely reported to affect cytotoxicity and protein biological activity,[38,39] their interactions with biological molecules such as proteins remain poorly understood at the molecular level. Furthermore, it remains unclear how the change in the secondary structure differs between the protein adsorbed on CB-NPs and unbound protein.

In this study, FTIR and CD spectroscopy were used to investigate the changes in the secondary structure of BSA upon adsorption onto CB-NPs (Printex 90 (P90), Printex 25 (P25), and Spezialschwarz 250 (S250)), which differ in size and surface properties. Albumin was selected as a protein with a high abundance in blood serum. Unbound and adsorbed proteins were separated to investigate CB-NP-induced differences in their secondary structure. In addition, molecular dynamics (MD) simulations were performed to investigate the effects of the CB-NP model with a diameter of 9 nm on the structure of a BSA monomer and associated intermolecular interactions. This combined experimental and computational study provides new insights into CB-NP-induced toxicity and associated protein–NP interactions.

Materials and methods

Materials

BSA and deuterium oxide (D_2O) were purchased from Sigma-Aldrich Co. (St. Louis, MO, USA). All CB-NPs (P90, P25, and S250) were purchased from Degussa Ltd (Frankfurt, Germany).

Characterization of CB-NPs

CB-NPs were prepared on a collodion-coated copper grid (Nissin-EM Co., Tokyo, Japan) and observed *via* transmission electron microscopy (TEM) (H-7650; Hitachi High-Tech Co., Tokyo, Japan). The primary particle size of CB-NPs was identified from the TEM images of >40 particles. The secondary particle size and zeta potential of CB-NPs dispersed in water were measured *via* dynamic light scattering (DLS) (ELSZ-2000ZS; Otsuka Electronics Co., Ltd, Osaka, Japan). Raman spectra of CB-NPs were measured using a microscopic laser Raman spectrometer (LabRAM HR-Evolution, HORIBA, Ltd, Kyoto, Japan) under excitation at 532 nm and 60 μW.

Fourier-transform infrared spectroscopy

FTIR is a widely used protein secondary structure analysis method for solvents and solids.[40–43] FTIR spectra along with amide bands were recorded on an FT/IR 6200 spectrometer (Shimadzu Co., Kyoto, Japan) for BSA (30 mg mL^{-1}) and CB-NPs (0.1 mg mL^{-1}) in D_2O following stirring for 48 h. D_2O was used as suspension media to avoid the overlap of the amide I band and strong absorption of water.[44,45] Ultrasonication was performed to improve the mixing of samples using an ultrasonic cleaner (CPX2800H-J, Emerson Japan, Ltd, Tokyo, Japan). Each sample was cast between two CaF_2 plates with a 25 μm spacer for liquid film FTIR analysis.

UV circular dichroism of BSA bound to CB-NPs

A mixture of BSA (30 mg mL^{-1}) and CB-NPs (0.1 mg mL^{-1}) was loaded onto a centrifugal filter column (molecular weight cut-off: 100 kDa; Merck Millipore Ltd, MA, USA) to remove BSA unbound to CB-NPs. The proteins that remained on and passed through the filter were denoted as "bound" and "unbound," respectively. The protein concentrations of "bound" and "unbound" samples were quantified using a BCA Protein Assay Kit (BioDynamics Laboratory Inc., Tokyo, Japan) based on the absorbance at 562 nm measured using a microplate reader (SH-9500; Corona Electric Co., Ltd, Ibaraki, Japan). Subsequently, CD analysis was performed on samples of bound BSA (diluted to 0.025 mg mL^{-1} with ultrapure water) in a quartz cell (optical path length: 10 mm; #83-1013; Sansyo Co., Ltd, Tokyo, Japan) using a circular dichroism spectrometer (J-820, JASCO Co., Tokyo, Japan).

MD simulations

Gromacs 2022.6 (ref. 46) was used to perform MD simulations using an Amber99SB forcefield. The simulations were performed in a simulation box of size $20 \times 20 \times 20$ nm^3. Three BSA monomers (PDB ID: 4f5s),[47] each with a total charge of −16, were inserted into the simulation box, maintaining the protein concentration at 40 mg mL^{-1}. Na^+ ions were added to neutralize the system. Considering the limitations of the simulation box size, a spherical CB-NP with a diameter of 9 nm was modeled with 1105 coronene molecules ($C_{24}H_{12}$). Coronene molecules with 96% carbon content were selected based on a previous modeling study of CB-NPs.[48] Notably, the experimentally observed density of our CB-NP model was 1.27 g cm^{-3}, which was lower than that of CB (1.7–1.9 g cm^{-3}).[49] The CB-NP model was inserted in the simulation box with an average initial distance of approximately 3 nm between the CB-NPs and BSA monomers. The systems were solvated in water using the TIP3P water model.

Four independent MD simulations were performed—starting from the energy minimization step performed with the steepest descent algorithm, followed by the constant-volume–constant-temperature (*NVT*) ensemble for 50 ps at a constant temperature of 298 K. Next, a constant-pressure–constant-temperature (*NPT*) equilibration step was performed for 50 ps with all-bond constraints at a constant pressure of 1 bar with a C-rescale barostat and V-rescale thermostat. MD production runs were performed with an integration time step of 2 fs at a constant pressure of 1 bar and constant temperature of 298 K using a Berendsen barostat and V-rescale thermostat. Periodic boundary conditions were applied in the *XYZ* directions and position restraints were set for coronene molecules.

To investigate the effect of CB-NPs on the BSA monomer, the binding of CB-NPs and at least one of the BSA monomers was achieved within 100 ns in two runs (runs #1 and #2). In addition, the binding of CB-NPs and two BSA monomers was achieved within 200 ns in the other two runs (runs #3 and #4). The changes in the intermolecular distances between the CB-NPs and BSA monomers within the production run were studied. The final 5 ns of the simulations were used to analyze the average root-mean-square fluctuations (RMSFs) of the carbon-alpha in the BSA monomers. In addition, the interactions between water molecules and BSA monomers were analyzed *via* radial distribution function (RDF) analyses performed in the last 5 ns of the simulations. The potential BSA to CB-NP binding sites were further studied considering three domains of BSA (domain I: amino-acid residue number (aa) 1–196, domain II: aa 204–381, and domain III: aa 382–571). The time evolution of the solvent-accessible surface area (SASA) of the BSA monomers was studied to characterize the changes observed in the protein structure. The simulation boxes were visualized using the visual molecular dynamics software.[50] The representative snapshots of the visualized simulation boxes at the beginning and end of simulations are shown in Fig. S1.

Results and discussion

CB-NP characterization

Characterization of CB-NPs was performed using DLS and TEM. DLS revealed that the peak average diameters of P90, P25, and S250 are 138.5, 154.9, and 148.6 nm, respectively (Fig. 1A). The zeta potential values for P90, P25, and S250 are −46.7, −51.5, and −61.0 mV, respectively, indicating that all particles are negatively charged (Fig. 1B). Notably, S250 exhibited relatively high dispersibility. P90 forms agglomeration of small

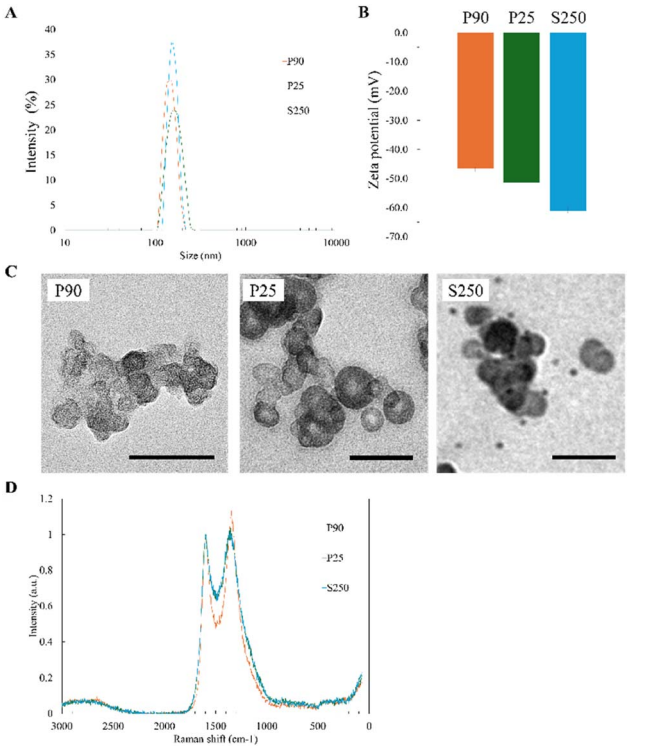

Fig. 1 Physicochemical characterization of carbon black nanoparticles (CB-NPs) (P90, P25, and S250). (A) Hydrodynamic diameter (secondary particle size) distributions determined by dynamic light scattering and (B) zeta potential of CB-NPs in an aqueous dispersion. (C) Representative transmission electron microscopy images showing nanoparticle morphologies of P90, P25, and S250. All scale bars represent 100 nm. (D) Raman spectra of three CB-NPs: P90, P25, and S250.

Table 1 Primary particle size of each carbon black nanoparticle (CB-NP) calculated from transmission electron microscopy images

Particle name	Primary size (nm)
P90	29.6 ± 7.90
P25	56.5 ± 19.8
S250	39.8 ± 9.10

individual particles, each of which is smaller than other particles (Fig. 1C and Table 1).

The results summarized in Table 1 indicate that P90 has the smallest primary particle size, whereas S250 has the largest size. The hydrodynamic secondary particle size determined by DLS shows that P90 has the smallest size, whereas S250 has the largest size for their agglomerations (Table 1). These results indicate that CB-NPs used in this study are available as models of environmental particles forming the typically structured clusters consisting of hundreds of spherical monomers with diameters in the range of 20–100 nm.[51]

Raman spectra in Fig. 1D show peaks at approximately 1350 cm^{-1} (D band) and 1600 cm^{-1} (G band) in all CB-NPs. P90 exhibits a higher D/G ratio and narrower Raman peaks than the others, suggesting that P90 has a crumbled structure owing to defects of the graphene lattice (Fig. 1D and Table 2).

FTIR spectra

Proteins show IR absorption, which is attributed to amide I and II vibrations (Fig. 2). Amide I absorption observed at approximately 1650 cm^{-1} and primarily attributed to C=O stretching vibrations was unaffected by the nature of the side chains but was dependent on the secondary structure of the primary chain. Therefore, it is commonly used in the secondary structure analysis.[52] The absorption peaks attributed to the conformational structure of BSA were amide II at 1570 cm^{-1}, intermolecular extended chains at 1613 cm^{-1}, β-sheet at 1628 cm^{-1}, α-helix at 1651 cm^{-1}, and β-turn at 1681 cm^{-1}.[52]

To quantitatively evaluate the absorption peaks attributed to each of these conformations, we performed peak separation by Gaussian fitting (Fig. 2B–E). The results reveal that the ratio of the α-helix or β-sheet in BSA does not change by mixing with any CB-NPs for 48 h (Fig. 2F), suggesting a negligible effect of CB-NPs on the secondary structure of BSA. These findings were in contrast with the results observed for TiO_2 NPs, which caused shifts in the α-helix and β-sheet peaks, suggesting a distortion in the BSA secondary structure upon adsorption.[53] Therefore, a critical difference in experimental conditions must be considered. Contrary to the use of dried solid samples for analysis in the previous study,[53] measurements in the current study were conducted in a liquid state (D_2O). The lyophilization process itself can potentially induce conformational changes in proteins, which may account for the discrepancy in the results obtained in the two studies.

Table 2 Raman spectroscopic parameters for CB-NPs

		Wave number		Half-width	
Particle name	D/G band	D band	G band	D band	G band
Printex 90	1.13	1344.02	1596.09	177.736	140.160
Printex 25	1.00	1363.98	1594.15	241.646	165.602
Spezialschwarz 250	1.03	1365.98	1599.97	241.646	167.530

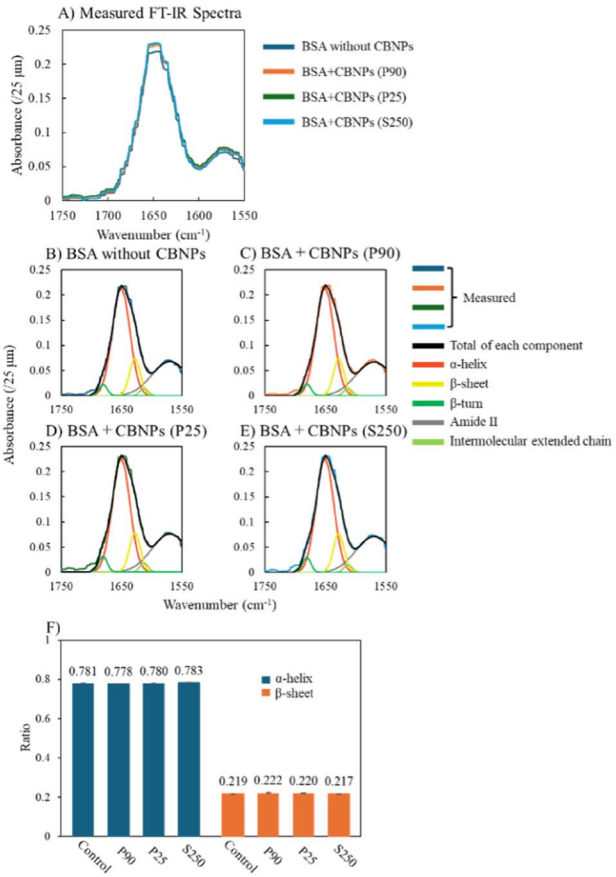

Fig. 2 Amide I band in Fourier transform infrared (FTIR) spectra of bovine serum albumin (BSA) interacting with CB-NPs. (A) FTIR spectra of BSA (30 mg mL^{-1}) and BSA on interaction with CB-NPs. (B–E) Deconvolution results *via* Gaussian fitting for the amide I band in FTIR spectra of BSA (30 mg mL^{-1}): (B) without NPs and with CB-NPs of (C) P90, (D) P25, and (E) S250. (F) Ratio of the α-helix and β-sheet in the amide I band of FTIR spectra of BSA incubated with CB-NPs.

Furthermore, the inherent structural stability of BSA is well-documented; this stability makes it resistant to significant conformational changes upon simple interaction with NPs. Notably, our results were consistent with the findings of Dasgupta *et al.*,[54] who also reported no significant alterations in the BSA secondary structure when interacting with silver NPs, as analyzed using FTIR. The results primarily suggested the secondary structure of excess BSA unbound to CB-NPs in the CB–BSA mixture. Furthermore, we examined the secondary structure change in BSA adsorbed upon interaction with NPs by excluding the unbound BSA in the CB–BSA mixture.

UV-CD spectra

To remove BSA unbound to CB-NPs from the CB–BSA mixture, the mixture samples were treated with a centrifugal column

filter. The BCA quantitative assay showed that, when 30 mg of BSA mixed with 0.1 mg of CB-NPs was applied to the filter, a total of 28.62 mg (95.4%), 29.13 mg (97.1%), and 28.35 mg (94.5%) of BSA were removed from the mixture as the protein unbound to P90, P25, and S250, respectively. The native BSA and BSA bound to CB-NPs (Fig. 3) were analyzed *via* UV-CD, which is a sensitive technique for studying conformational changes in proteins.

Previous studies determined the α-helix content—the dominant structure in albumin based on the interpretation of CD spectroscopy by analyzing changes at 207–209 nm and 222 nm.[55–57] β-sheet structures exhibited a negative peak at 216 nm,[58] while the negative peak of BSA at 207–209 nm did not exhibit any shift when the protein retained its predominant α-helix structure without unfolding.[37] In our results with CB-NPs, the negative peak at approximately 207 nm shifts to longer wavelengths and the peak at approximately 215–222 nm becomes flat in the BSA bound to P90 (Fig. 3D), suggesting that only this sample causes slight denaturation of the protein secondary structure. The changes in CD of BSA bound to P90 suggested an α-helix decrease and a β-sheet increase. These changes were not observed in BSA with the other CB-NPs.

In CB, the six- and five-membered carbon rings formed a pseudo-graphite structure, and their aggregates formed primary particles, which in turn formed primary aggregates that are the smallest units of CB.[59] The Raman spectra suggested a higher number of defects in the graphene structure in P90 than in other CB-NPs. In addition, P90 exhibited the smallest primary particle size (Table 1) with the largest curvature (radius of curvature: 14.8 (±3.95) nm as spherical NPs). Reportedly, the large curvature of CB-NPs also induces conformational changes in proteins.[60] The larger curvature of NPs is expected to increase the number of binding sites of a protein to NPs during adsorption, which may lead to the exposure of originally buried amino acid residues and physical conformational changes caused by binding. There is still a limitation that the effects of CB-NPs with the same surface chemistry and varied sizes are not directly compared yet. Further investigations are expected *via* preparing such CB-NPs in future studies.

In summary, analysis of the secondary structure of BSA-which contains both fractions unbound and bound to CB-NPs-using FT-IR[44] in the present study was consistent with that in previous studies,[35] which reported that these structural changes were not observed by UV-CD. In a previous study, CD analysis of BSA (0.01 M) incubated for 2 h with CB-NPs (0.01 or 0.02 mg mL^{-1}) did not exhibit any changes in the characteristic range of 207–209 nm and 222 nm negative peaks of α-helix,[35] indicating that the native conformation was retained. The present study newly reported that the changes were observed only when the unbound fraction was removed to concentrate the bound (adsorbed) fraction onto P90 and the UV-CD spectral changes were observed.

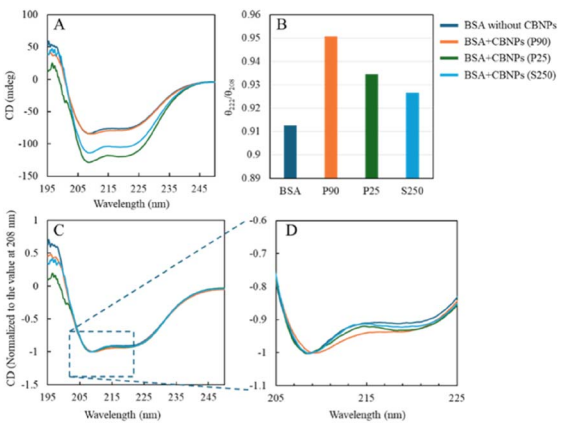

Fig. 3 Conformational changes of BSA upon adsorption onto CB-NPs, analyzed by circular dichroism (CD) spectroscopy. (A) CD spectra of native BSA and BSA adsorbed on the three types of CB-NPs (P90, P25, and S250) after removal of the unbound protein. (B) Ratio of the CD signal from 222 to 208 nm, which serves as an indicator of α-helical content of BSA. (C) CD spectra from (A) normalized at 208 nm to facilitate comparison of spectral shapes. (D) An enlarged view of normalized spectra in (C), highlighting a red-shift at approximately 208 nm and a reduction in the negative signal at 222 nm, indicating structural changes in BSA upon adsorption.

MD simulations

MD simulations were further performed to investigate the effect of the 9 nm CB-NP model on the BSA monomers and associated intermolecular interactions. Considering the limitations of the simulation box of size 20 × 20 × 20 nm^3, a CB-NP model of 9 nm was used in our simulations. The three BSA monomers present in each simulation box were numbered BSA #1, #2, and #3 to distinguish them. As shown in Fig. 4, one BSA monomer is adsorbed on the surface of CB-NPs within 100 ns in runs #1 and #2, whereas two BSA monomers are adsorbed on the CB-NPs within 200 ns in runs #3 and #4. The interactions between BSA monomers and water are studied at the end of the simulations *via* RDF analysis, as shown in Fig. 5. As shown in Fig. 5, the BSA monomers adsorbed on the surface of CB-NPs exhibit decreased interactions with water, as indicated by a decrease in the RDF peaks. In particular, in run #1, decreased RDF

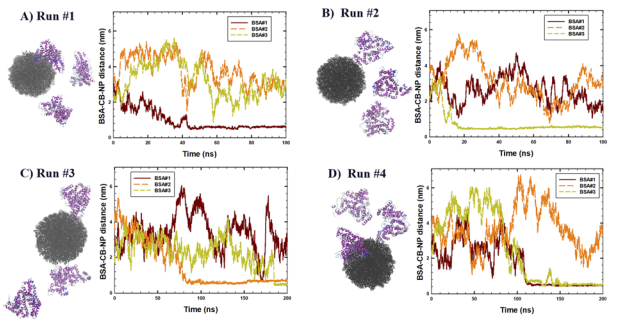

Fig. 4 Time-evolution of distances between CB-NPs and the three BSA monomers with representative snapshots of systems at the end of corresponding MD simulations: runs (A) #1, (B) #2, (C) #3, and (D) #4. Water molecules and ions are not shown for clarity. Coloring methods: black: 9 nm CB-NP model; the secondary structure of BSA protein: blue and violet: helices and white and cyan: unstructured bend and turn.

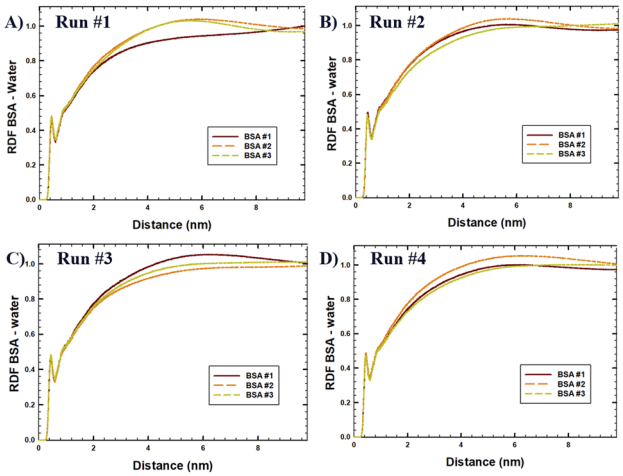

Fig. 5 Radial distribution functions of interactions between water and BSA monomers in the last 5 ns of simulations in each run: (A) #1, (B) #2, (C) #3, and (D) #4.

interactions at a distance of 2 nm and further are observed between water and BSA #1 (Fig. 5A), which is adsorbed on the surface of the CB-NPs (Fig. 4A).

Similarly, in all runs, the adsorbed BSA monomers exhibited reduced interactions with water molecules beyond a distance of 2 nm, particularly BSA #3 in run #2, BSA #2 and #3 in run #3, and BSA #1 and #3 in run #4 (Fig. 5B–D). However, the first hydration shell of BSA monomers remained unaffected by the adsorption on the CB-NPs because no difference was observed at a distance of 0.4 nm in the RDF plots.

To investigate the preferable binding sites of BSA on the surface of the CB-NP model, we studied the time evolution of the distances between CB-NPs and protein domains for the BSA monomers adsorbed on the CB-NPs, as shown in Fig. 6. According to Fig. 6A, the BSA monomer was adsorbed on the surface of CB-NPs *via* domains I and III in run #1, as shown by low intermolecular distance with values at approximately 0.7 and 0.6 nm, respectively. In run #2, the BSA monomer is adsorbed on the surface of CB-NPs *via* domain III (Fig. 6B).

In run #3, one of the BSA monomers is adsorbed on the surface of the CB-NPs with domains II and III (Fig. 6C), whereas another monomer is bound with domain II (Fig. 6D). In run #4, one of the BSA monomers is adsorbed onto domain III (Fig. 6E), whereas the other monomer is bound on the surface of the CB-NPs *via* domain I (Fig. 6F). Although no specific binding sites were observed, domain III had a higher occurrence of being adsorbed on the surface of the CB-NP model. In particular, 4 out of 6 BSA monomers were adsorbed to CB-NPs with domain III. These observations were in agreement with the results of an earlier MD study,[61] which reported that the BSA subdomain IIIA (of domain III) was adsorbed with high hydrophobicity on the graphite surface.

Furthermore, the last 5 ns of simulations were used to analyze the average RMSF fluctuations of the carbon-alpha in the BSA monomers (Fig. 7) to characterize the movement of amino acid residues upon adsorption on the surface of CB-NPs. As shown in Fig. 7A, the adsorption of the BSA #1 monomer resulted in the suppressed movement of the amino acids in run #1, with a more significant decrease in the RMSF values at 0.2 nm in domains II and III. The results indicated decreased protein mobility owing to the binding of domains I and III to the CB-NPs. In run #2, decreased RMSF fluctuations in domains I and III (down to 0.2 and 0.3 nm, respectively) are observed in BSA #3 owing to the adsorption of domain III on the surface of CB-NPs (Fig. 7B). Furthermore, in run #3, decreased protein mobility of all domains was observed in BSA #2 (at 0.2 nm), which was adsorbed *via* domains II and III (Fig. 7C). In comparison, a decrease in the RMSF values in domains II and III (at 0.2 nm) was observed in BSA #3 owing to the adsorption of domain II on the surface of CB-NPs. In run #4 (Fig. 7D), decreased RMSF fluctuations in domain III (at 0.3 nm) were observed in BSA #1 owing to the adsorption of domain III on the surface of CB-NPs. In contrast, increased RMSF values in domains I and III (up to 1.2 nm) were observed in BSA #3 owing to the adsorption of domain I on the CB-NPs, indicating high protein mobility. Although increased RMSF fluctuations could be observed during the adsorption of domain I (run #4 and BSA #3) on the surface of CB-NPs, in general, decreased mobility of

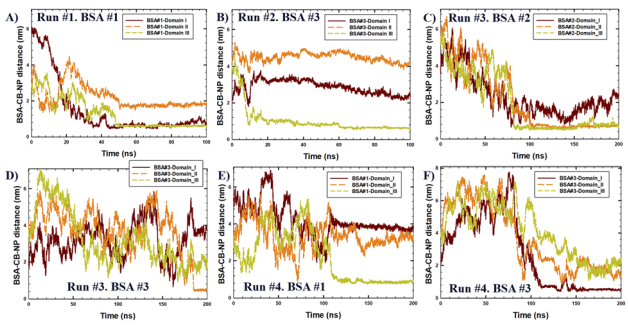

Fig. 6 Time-evolution of distances between CB-NPs and BSA monomer domains of adsorbed monomers in each run: (A) run #1 – BSA#1, (B) run #2 – BSA #3, (C) run #3 – BSA #2, (D) run #3 – BSA #3, (E) run #4 – BSA #1, and (F) run #4 – BSA #3.

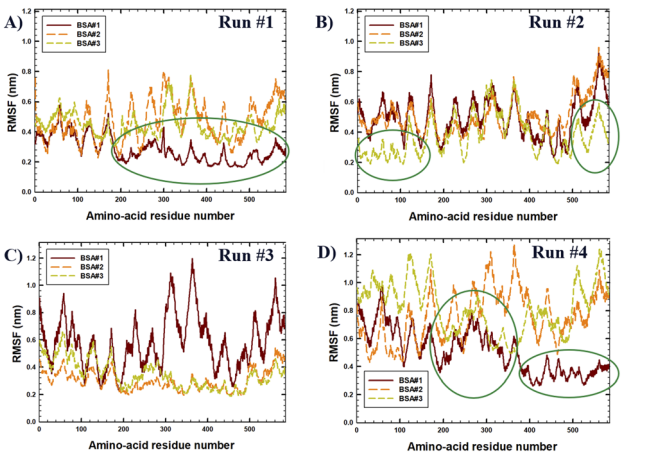

Fig. 7 Root-mean-square fluctuations of BSA monomers averaged for the last 5 ns of simulations in each run: runs (A) #1, (B) #2, (C) #3, and (D) #4.

the amino acids was observed due to protein adsorption, with a more significant effect during the simultaneous adsorption of domains II and III (in BSA #2 and run #3).

Furthermore, the effect of the CB-NP model on the SASA of the BSA protein was studied; however, no significant effect was observed within the simulated time. The results of the SASA analysis are shown in Fig. S2 and S3.

Overall, the results of our MD simulations revealed that the BSA monomers might be adsorbed on the surface of the CB-NPs owing to hydrophobic interactions. Although no specific binding sites were revealed and all three domains of BSA could be adsorbed on the surface of the CB-NP model, domain III had a higher propensity to be adsorbed. Furthermore, upon being adsorbed on the surface of CB-NPs, the fluctuations in the amino acid positions generally decreased, which was attributed to the strong binding to CB-NPs and decreased protein mobility. Moreover, CB-NPs might have enhanced the formation of protein aggregates by serving as a surface for the adsorption of proteins.

Finally, some limitations regarding this study merit discussion. The concentration dependence, which could not be investigated in this study, is not simple and is also biased by the adsorption affinity between NPs and proteins. As the NP concentration increases, the NP surface area within the system increases, leading to a decrease in the density of proteins adsorbed onto the NP surface and a weakening in their interactions.[45] Previous studies have shown that the adsorption behavior of proteins onto NP surfaces depends not only on surface chemistry but also on surface morphology and roughness related to NP size.[73] A detailed investigation into the relation between changes in BSA adsorption due to NP size and changes in decreased secondary structure will be the subject in future studies.

Conclusions

Changes in the secondary structure of BSA were not detected in the FTIR measurements after 48 h of interaction with CB-NPs. However, a minimal change might be observed in BSA incubated with P90, which had a more defective graphene structure and the smallest primary particle size compared to other CB-NPs. This limitation was possibly attributed to the coexistence of a large amount of unbound BSA that did not interact with CB-NPs in the sample. The CD spectrum of BSA adsorbed onto P90 exhibited a slight variation, suggesting that the secondary structure of only the BSA adsorbed onto a CB-NP with the defective graphene structure was affected. Furthermore, the results of our MD simulations revealed that the strong binding of BSA monomers to CB-NPs decreased protein mobility, suggesting that CB-NPs might serve as a surface for the adsorption of proteins. Although no specific binding sites of the BSA monomer to the CB-NP model were revealed, domain III had a higher propensity for adsorption. Overall, the proteins adsorbed onto NPs should be isolated to reveal the conformational changes in the protein caused by CB-NPs dependent on their surface properties. These NP–protein interactions may lead to the elucidation of biological and health-related effects of NPs by clarifying their effect on the *in vivo* function, stability, and degradability of proteins.

Author contributions

Project administration and conceptualization, MU; supervision, MU and TW; methodology, YT, SK, NS, and MU; investigation & formal analysis, YT, SK, and AT; validation & visualization, YT, SK, and MU; funding acquisition, AO and MU; writing – original draft, YT and SK; writing – review & editing, MU and AO.

Conflicts of interest

The authors have no conflicts of interest to declare.

Data availability

Data to reproduce the figures of this article are available at https://tus.box.com/s/5fxpvrbkakzj3ia2t6r2dbowanb41was.

Supplementary information (SI): Fig. S1: visualized simulation boxes at the beginning and the end of the MD simulations. Fig. S2: the solvent-accessible surface area of three BSA monomers in runs #1 and #2. Fig. S3: the solvent-accessible surface area of three BSA monomers in runs #3 and #4. See DOI: https://doi.org/10.1039/d5em00868a.

Acknowledgements

This work was in part supported by the JST FOREST Program (Grant Number JPMJFR225B), JSPS KAKENHI (Grant Numbers 23K18403, 22H03335 and 25K02871), and The Kato Memorial Bioscience Foundation.

Notes and references

1 T. T. Chen, K. J. Chuang, L. L. Chiang, C. C. Chen, C. T. Yeh, L. S. Wang, C. Gregory, T. Jones, K. BéruBé, C. N. Lee, H. C. Chuang and T. J. Cheng, Characterization of the interactions between protein and carbon black, *J. Hazard. Mater.*, 2014, **264**, 127–135.

2 D. H. K. Nguyen, V. T. H. Pham, M. Al Kobaisi, C. Bhadra, A. Orlowska, S. Ghanaati, B. M. Manzi, V. A. Baulin, S. Joudkazis, P. Kingshott, R. J. Crawford and E. P. Ivanova, Adsorption of human plasma albumin and fibronectin onto nanostructured black silicon surfaces, *Langmuir*, 2016, **32**, 10744–10751.

3 I. Lynch and L. A. Dawson, Protein-nanoparticle interactions, *Nanotoday*, 2008, **3**, 40–47.

4 R. Podila, P. Vedantam, P. C. Ke, J. M. Brown and A. M. Rao, Evidences for charge transfer-induced conformational changes in carbon nanostructure-protein corona, *J. Phys. Chem. C*, 2012, **116**, 22098–22103.

5 S. I. Soneja, J. M. Tielsch, F. C. Curriero, B. Zaitchik, S. K. Khatry, B. Yan, S. N. Chillrud and P. N. Breysse, Determining particulate matter and black carbon exfiltration estimates for traditional cookstove use in rural

Nepalese village households, *Environ. Sci. Technol.*, 2015, **49**, 5555–5562.

6 O. S. Patange, N. Ramanathan, I. H. Rehman, S. N. Tripathi, A. Misra, A. Kar, E. Graham, L. Singh, R. Bahadur and V. Ramanathan, Reductions in indoor black carbon concentrations from improved biomass stoves in rural India, *Environ. Sci. Technol.*, 2015, **49**, 4749–4756.

7 D. P. Bhatt, K. L. Puig, M. W. Gorr, L. E. Wold and C. K. Combs, A pilot study to assess effects of long-term inhalation of airborne particulate matter on early Alzheimer-like changes in the mouse brain, *PLoS One*, 2015, **10**, e0127102.

8 S. J. Park, J. Lee, S. Lee, S. Lim, J. Noh, S. Y. Cho, J. Ha, H. Kim, C. Kim, S. Park, D. Y. Lee and E. Kim, Exposure of ultrafine particulate matter causes glutathione redox imbalance in the hippocampus: A neurometabolic susceptibility to Alzheimer's pathology, *Sci. Total Environ.*, 2020, **718**, 137267.

9 A. Onoda, T. Kawasaki, K. Tsukiyama, K. Takeda and M. Umezawa, Perivascular accumulation of β-sheet-rich proteins in offspring brain following maternal exposure to carbon black nanoparticles, *Front. Cell. Neurosci.*, 2017, **11**, 92.

10 M. Riediker, D. Zink, W. Kreyling, G. Oberdörster, A. Elder, U. Graham, I. Lynch, A. Duschl, G. Ichihara, S. Ichihara, T. Kobayashi, N. Hisanaga, M. Umezawa, T. J. Cheng, R. Handy, M. Gulumian, S. Tinkle and F. Cassee, Particle toxicology and health - where are we?, *Part. Fibre Toxicol.*, 2019, **16**, 19.

11 A. Onoda, T. Kawasaki, K. Tsukiyama, K. Takeda and M. Umezawa, Carbon nanoparticles induce endoplasmic reticulum stress around blood vessels with accumulation of misfolded proteins in the developing brain of offspring, *Sci. Rep.*, 2020, **10**, 10028.

12 A. Onoda, M. Umezawa, K. Takeda, T. Ihara and M. Sugamata, Effects of maternal exposure to ultrafine carbon black on brain perivascular macrophages and surrounding astrocytes in offspring mice, *PLoS One*, 2014, **9**, e94336.

13 A. Onoda, K. Takeda and M. Umezawa, Dose-dependent induction of astrocyte activation and reactive astrogliosis in mouse brain following maternal exposure to carbon black nanoparticle, *Part. Fibre Toxicol.*, 2017, **14**, 4.

14 M. Umezawa, A. Onoda, I. Korshunova, A. C. Ø. Jensen, I. K. Koponen, K. A. Jensen, K. Khodosevich, U. Vogel and K. S. Hougaard, Maternal inhalation of carbon black nanoparticles induces neurodevelopmental changes in mouse offspring, *Part. Fibre Toxicol.*, 2018, **15**, 36.

15 C. S. Yah, G. S. Simate and S. E. Iyuke, Nanoparticles toxicity and their routes of exposures, *Pak. J. Pharm. Sci.*, 2012, **25**, 477–491.

16 G. Fullstone, J. Wood, M. Holcombe and G. Battaglia, Modelling the Transport of nanoparticles under blood flow using an agent-based approach, *Sci. Rep.*, 2015, **5**, 10649.

17 G. G. De La Cruz, P. Rodríguez-Fragoso, J. Reyes-Esparza, A. Rodríguez-López, R. Gómez-Cansino and L. Rodriguez-Fragoso, Interaction of nanoparticles with blood components and associated pathophysiological effects, in *Unraveling the Safety Profile of Nanoscale Particles and Materials—From Biomedical to Environmental Applications*, 2018, pp. 37–59.

18 M. Mahmoudi, S. Laurent, M. A. Shokrgozar and M. Hosseinkhani, Toxicity evaluations of superparamagnetic iron oxide nanoparticles: cell "vision" versus physicochemical properties of nanoparticles, *ACS Nano*, 2011, **5**, 7263–7276.

19 M. Rabe, D. Verdes and S. Seeger, Understanding protein adsorption phenomena at solid surfaces, *Adv. Colloid Interface Sci.*, 2011, **162**, 87–106.

20 L. M. Pandey and S. K. Pattanayek, Properties of competitively adsorbed BSA and fibrinogen from their mixture on mixed and hybrid surfaces, *Appl. Surf. Sci.*, 2013, **264**, 832–837.

21 L. M. Pandey and S. L. Pattanayek, Relation between the wetting effect and the adsorbed amount of water-soluble polymers or proteins at various interfaces, *J. Chem. Eng. Data*, 2013, **58**, 3440–3446.

22 Z. J. Deng, M. Liang, M. Monteiro, I. Toth and R. F. Minchin, Nanoparticle-induced unfolding of fibrinogen promotes Mac-1 receptor activation and inflammation, *Nat. Nanotechnol.*, 2011, **6**, 39–44.

23 C. Palocci, L. Chronopoulou, I. Venditti, E. Cernia, M. Diociaiuti, I. Fratoddi and M. V. Russo, Lipolytic enzymes with improved activity and selectivity upon adsorption on polymeric nanoparticles, *Biomacromolecules*, 2007, **8**, 3047–3053.

24 M. Mahmoudi, M. A. Shokrgozar, S. Sardari, M. K. Moghadam, H. Vali, S. Laurentc and P. Stroeve, Irreversible changes in protein conformation due to interaction with superparamagnetic iron oxide nanoparticles, *Nanoscale*, 2011, **3**, 1127–1138.

25 M. Holmberg and X. Hou, Competitive protein adsorption–multilayer adsorption and surface induced protein aggregation, *Langmuir*, 2009, **25**, 2081–2089.

26 M. Holmberg, K. B. Stibius, N. B. Larsen and X. Hou, Competitive protein adsorption to polymer surfaces from human serum, *J. Mater. Sci.:Mater. Med.*, 2008, **19**, 2179–2185.

27 C. M. Alves, R. L. Reis and J. A. Hunt, The competitive adsorption of human proteins onto natural-based biomaterials, *J. R. Soc. Interface*, 2010, **7**, 1367–1377.

28 J. Benesch, J. F. Mano and R. L. Reis, Analysing protein competition on self-assembled mono-layers studied with quartz crystal microbalance, *Acta Biomater.*, 2010, **6**, 3499–3505.

29 A. Hasan, G. Waibhaw and L. M. Pandey, Conformational and Organizational Insights into Serum Proteins during Competitive Adsorption on Self-Assembled Monolayers, *Langmuir*, 2018, **34**, 8178–8194.

30 L. M. Pandey, S. K. Pattanayek and D. Delabouglise, Properties of Adsorbed Bovine Serum Albumin and Fibrinogen on Self-Assembled Monolayers, *J. Phys. Chem. C*, 2013, **117**, 6151–6160.

31 L. Treuel, M. Malissek, J. S. Gebauer and R. Zellner, The influence of surface composition of nanoparticles on their interactions with serum albumin, *ChemPhysChem*, 2010, **11**, 3093–3099.
32 R. E. Cristian, I. J. Mohammad, M. Mernea, B. G. Sbarcea, B. Trica, M. S. Stan and A. Dinischiotu, Analyzing the interaction between two different types of nanoparticles and serum albumin, *Materials*, 2019, **12**, 3183.
33 M. Umezawa, R. Itano, N. Sakaguchi and T. Kawasaki, Infrared spectroscopy analysis determining secondary structure change in albumin by cerium oxide nanoparticles, *Frontiers in Toxicology*, 2023, **5**, 1237819.
34 A. Rajeshwari, S. Pakrashi, S. Dalai, Madhumita, V. Iswarya, N. Chandrasekaran and A. Mukherjee, Spectroscopic studies on the interaction of bovine serum albumin with Al_2O_3 nanoparticles, *J. Lumin.*, 2014, **145**, 859–865.
35 H. Wu, M. Chen, M. Shang, X. Li, K. Mu, S. Fan, S. Jiang and W. Li, Insights into the binding behavior of bovine serum albumin to black carbon nanoparticles and induced cytotoxicity, *Spectrochim. Acta, Part A*, 2018, **200**, 51–57.
36 L. Li, R. Lin, H. He, M. Sun, L. Jiang and M. Gao, Interaction of amidated single-walled carbon nanotubes with protein by multiple spectroscopic methods, *J. Lumin.*, 2014, **145**, 125–131.
37 J. Kuchlyan, N. Kundu, D. Banik, A. Roy and N. Sarkar, Spectroscopy and fluorescence lifetime imaging microscopy to probe the interaction of bovine serum albumin with graphene oxide, *Langmuir*, 2015, **31**, 13793–13801.
38 H. Wu, L. Lin, P. Wang, S. Jiang, Z. Dai and X. Zou, Solubilization of pristine fullerene by the unfolding mechanism of bovine serum albumin for cytotoxic application, *Chem. Commun.*, 2011, **47**, 10659–10661.
39 C. Chung, Y. K. Kim, D. Shin, S. R. Ryoo, B. H. Hong and D. H. Min, Biomedical applications of graphene and graphene oxide, *Acc. Chem. Res.*, 2013, **46**, 2211–2224.
40 Y. Jiang, C. Li, X. Nguyen, S. Muzammil, E. Towers, J. Gabrielson and L. Narhi, Qualification of FTIR spectroscopic method for protein secondary structural analysis, *J. Pharm. Sci.*, 2011, **100**, 4631–4641.
41 J. Zhang, X. Zhang, F. Zhang and S. Yu, Solid-film sampling method for the determination of protein secondary structure by Fourier transform infrared spectroscopy, *Anal. Bioanal. Chem.*, 2017, **409**, 4459–4465.
42 J. D'antonio, B. M. Murphy, M. C. Manning and W. A. Al-Azzam, Comparability of protein therapeutics: quantitative comparison of second-derivative amide I infrared spectra, *J. Pharm. Sci.*, 2012, **101**, 2025–2033.
43 J. Kong and S. Yu, Fourier transform infrared spectroscopic analysis of protein secondary structures, *Acta Biochim. Biophys. Sin.*, 2007, **39**, 549–559.
44 M. J. Krysmann, V. Castelletto, A. Kelarakis, I. W. Hamley, R. A. Hule and D. J. Pochan, Self-assembly and hydrogelation of an amyloid peptide fragment, *Biochemistry*, 2008, **47**, 4597–4605.
45 N. Sakaguchi, S. Kaumbekova, R. Itano, M. A. Torkmahalleh, D. Shah and M. Umezawa, Changes in the secondary structure and assembly of proteins on fluoride ceramic (CeF_3) nanoparticle surfaces, *ACS Appl. Bio Mater.*, 2022, **5**, 2843–2850.
46 M. J. Abraham, T. Murtola, R. Schulz, S. Páll, J. C. Smith, B. Hess and E. Lindahl, GROMACS: High performance molecular simulations through multi-level parallelism from laptops to supercomputers, *SoftwareX*, 2015, **1–2**, 19–25.
47 A. Bujacz, Structures of bovine, equine and leporine serum albumin, *Acta Crystallogr., Sect. D:Biol. Crystallogr.*, 2012, **68**, 1278–1289.
48 S. Ban, K. Malek, C. Huang and Z. Liu, A molecular model for carbon black primary particles with internal nanoporosity, *Carbon*, 2011, **49**, 3362–3370.
49 C. M. Long, M. A. Nascarella and P. A. Valberg, Carbon black vs. black carbon and other airborne materials containing elemental carbon: Physical and chemical distinctions, *Environ. Pollut.*, 2013, **181**, 271–286.
50 W. Humphrey, A. Dalke and K. Schulten, VMD: visual molecular dynamics, *J. Mol. Graphics*, 1996, **14**, 33.
51 N. Moteki, Discrete dipole approximation for black carbon-containing aerosols in arbitrary mixing state: A hybrid discretization scheme, *J. Quant. Spectrosc. Radiat. Transfer*, 2016, **178**, 306–314.
52 A. Barth and C. Zscherp, What vibrations tell us about proteins, *Q. Rev. Biophys.*, 2002, **35**, 369–430.
53 S. Ranjan, N. Dasgupta, P. Srivastava and C. Ramalingam, A spectroscopic study on interaction between bovine serum albumin and titanium dioxide nanoparticle synthesized from microwave-assisted hybrid chemical approach, *J. Photochem. Photobiol., B*, 2016, **161**, 472–481.
54 N. Dasgupta, S. Ranjan, D. Patra, P. Srivastava, A. Kumar and C. Ramalingam, Bovine serum albumin interacts with silver nanoparticles with a "side-on" or "end on" conformation, *Chem.-Biol. Interact.*, 2016, **253**, 100–111.
55 L. Shang, Y. Wang, J. Jiang and S. Dong, pH-Dependent Protein Conformational Changes in Albumin:Gold Nanoparticle Bioconjugates: A Spectroscopic Study, *Langmuir*, 2007, **23**, 2714–2721.
56 Q. Xiao, S. Huang, Y. Liu, F. F. Tian and J. C. Zhu, Thermodynamics, conformation and active sites of the binding of Zn–Nd hetero-bimetallic Schiff base to bovine serum albumin, *J. Fluoresc.*, 2009, **19**, 317–326.
57 Y. Li, W. He, J. Tian, J. Tang, Z. Hu and X. Chen, The effect of Berberine on the secondary structure of human serum albumin, *J. Mol. Struct.*, 2005, **743**, 79–84.
58 R. Townend, T. F. Kumosinski, S. N. Timasheff, G. D. Fasman and B. Davidson, The circular dichroism of the beta structure of poly-L-lysine, *Biochem. Biophys. Res. Commun.*, 1966, **23**, 163–169.
59 J. López-de-Uralde, I. Ruiz, I. Santos, A. Zubillaga, P. G. Bringas, A. Okariz and T. Graya, utomatic Morphological categorisation of carbon black nano-aggregates, in *DEXA 2010, Part II, LNCS 6262*, 2010, pp. 185–193.
60 P. Roach, D. Farrar and C. C. Perry, Surface tailoring for controlled protein adsorption: effect of topography at the

nanometer scale and chemistry, *J. Am. Chem. Soc.*, 2006, **3939**, 128.

61 C. Mücksch and H. M. Urbassek HM, Molecular dynamics simulation of free and forced BSA adsorption on a hydrophobic graphite surface, *Langmuir*, 2001, **27**, 12938.

62 H. A. Housseiny, M. Singh, S. Emile, M. Nicoleau, R. L. V. Wal and P. Silveyra, Identification of toxicity parameters associated with combustion produced soot surface chemistry and particle structure by in vitro assays, *Biomedicines*, 2020, **8**, 345.

63 N. Dridi, Z. Jin, W. Perng and H. Mattoussi, Probing protein corona formation around gold nanoparticles: Effects of surface coating, *ACS Nano*, 2024, **18**, 8649–8662.

64 W. Wang, R. Lei, L. Li, X. Fei, R. Ju, X. Sun, H. Cao, Q. Zhang, C. Chen and X. Wang, *Nanoscale*, 2021, **13**, 20425–20436.

65 M. Mehrabi, M. F. Ghasemi, B. Rasti, M. Falahati, A. Mirzaie and A. Hasan, Nanoporous iron oxide nanoparticle: hydrothermal fabrication, human serum albumin interaction and potential antibacterial effects, *J. Biomol. Struct. Dyn.*, 2021, **39**, 2595–2606.

66 A. Nisar, D. K. Ajabia, S. B. Agrawal, S. Varma, B. P. Chaudhari and R. S. Tupe, Mechanistic insight into differential interactions of iron oxide nanoparticles with native, glycated albumin and their effect on erythrocytes parameters, *Int. J. Biol. Macromol.*, 2022, **212**, 232–247.

67 S. Kaumbekova, N. Sakaguchi N, D. Shah and M. Umezawa, Effect of gold nanoparticles on the conformation of bovine serum albumin: Insights from CD spectroscopic analysis and molecular dynamics simulations, *ACS Omega*, 2024, **9**, 49283–49292.

68 S. Kaumbekova, K. Omata, R. Nagasawa and M. Umezawa, Effect of gold nanoparticles and coexisting acetonitrile solvent on the structure of bovine serum albumin, *ACS Omega*, 2025, **10**, 48370–48384.

69 M. Bukackova and R. Marsalek, Interaction of BSA with ZnO, TiO2, and CeO2 nanoparticles, *Biophys. Chem.*, 2020, **267**, 106475.

70 L. F. Ferreira, A. S. Picco, F. E. Galdino, L. J. C. Albuquerque, J.-F. Berret and M. B. Cardoso, Nanoparticle–protein interaction: Demystifying the correlation between protein corona and aggregation phenomena, *ACS Appl. Mater. Interfaces*, 2022, **14**, 28559–28569.

71 V. Francia, K. Yang, C. Reker-Smit, I. Nelissen and A. Salvati, Corona composition can affect the mechanisms cells use to internalize nanoparticles, *ACS Nano*, 2019, **13**, 11107–11121.

72 P. Dalhaimer, B. Florey and S. Isaac, Interactions of apolipoproteins with lipid-based nanoparticles, *ACS Nano*, 2023, **17**, 837–842.

73 N. T. Co and M. S. Li, Effect of surface roughness on aggregation of polypeptide chains: A monte Carlo study, *Biomolecules*, 2021, **11**, 596.

